

Research Article

Corrosion Behaviors of Microarc Oxidation Coating and Anodic Oxidation on 5083 Aluminum Alloy

Haiou Sun,¹ Liangcai Li,¹ Zhongyi Wang ¹, Bin Liu ^{1,2}, Meng Wang,¹ and Yunliang Yu¹

¹College of Power and Energy Engineering, Harbin Engineering University, Harbin, China

²Corrosion and Protection Laboratory, Key Laboratory of Superlight Materials and Surface Technology, Harbin Engineering University, Ministry of Education, Harbin, China

Correspondence should be addressed to Zhongyi Wang; b205030024@126.com and Bin Liu; liubin@hrbeu.edu.cn

Received 28 March 2020; Revised 15 October 2020; Accepted 24 October 2020; Published 21 November 2020

Academic Editor: Jian Chen

Copyright © 2020 Haiou Sun et al. This is an open access article distributed under the Creative Commons Attribution License, which permits unrestricted use, distribution, and reproduction in any medium, provided the original work is properly cited.

The microarc oxidation (MAO) coating and anodic oxidation coating were prepared on 5083 aluminum alloy. The surface morphology, elemental composition, and electrochemical behavior of the two coatings were analyzed. The results proved that the corrosion resistance of the MAO coating is superior than that of the anodic oxidation coating. The protective ability of the coating deteriorated gradually with the increase in immersion time. The corrosion process is controlled by ion diffusion throughout the coatings.

1. Introduction

The air intake filter is generally equipped in front of the gas turbine to filter out the salt sprays contained in the intake airflow, and thus, the service life of the gas turbine could be effectively guaranteed and extended [1–5]. In order to meet the requirements of high efficiency and low resistance of the air intake filter, the cyclone filter usually serves as the first stage. The cyclone filter is generally exposed to the marine atmosphere and is susceptible to corrosion due to the salt spray particles of the marine environment [6–11]. In addition, to reduce the weight and the quality control cost of the cyclone filter and its components, the cyclone filter is generally made from aluminum alloy [6, 12]. The surface coating technology is an effective and economical way to enhance the anticorrosion resistance of the aluminum alloy substrate [13]. Therefore, the surface coating technology and the degradation behaviors of the cyclone separators in corrosive environment are the necessary guarantee for the safe operation of the cyclone separators. So the research and development of the surface coating technology for aluminum alloy has important significance.

Since the 1970s, a large amount of literatures concentrated on the cyclone separators have been published.

Tabakoff and Grant [14] proposed a purely empirical formula to describe the collisional motion between the particles and the wall. Kim and Lee [15] developed a two-phase flow model to investigate the sedimentation and turbulent diffusion effects of solid particles in the boundary layer. Brouwers [16] used the numerical and experimental method to investigate the separation efficiency of the rotational axial-flow separator. Zhang et al. [17] conducted an experimental research on an axial-flow multitube cyclone separator. The results indicated that the axial-flow multitube cyclone has a higher separation efficiency and lower resistance than the tangential inlet cyclone. However, aluminum and aluminum alloys are reported to corrode mainly in the forms of pitting, intergranular corrosion (IGC), and stress corrosion cracking (SCC), when they are exposed to the solutions containing chloride ions [18–23]. Al coating, i.e., microarc oxidation (MAO) and anodic oxidation coating, can significantly improve the anticorrosion resistance of the aluminum alloys. Wang et al. [24] investigated a ceramic coating deposited on Al matrix composite by MAO and found that surface hardness wear resistance of the composite can be significantly improved. Chen et al. [25] investigated the corrosion performance of MAO coatings on different regions of the friction stirred 6061 aluminum alloy plate and found that the

corrosion protection performance of the MAO coating can be improved by inducing the coarse and congregated Al-Fe-Si particles into fine and disperse distributed particles. Krishtal [26] found that the substantial improvement in corrosion resistance of the friction stir welds of 7075 aluminum alloy can be achieved by MAO treatment. Xin et al. [27] investigated the properties of alumina coatings prepared by the MAO process using direct current (DC) and unbalanced alternative current (AC) power supplies. The results showed that the coating deposited by AC possesses higher density, hardness, and corrosion resistance. Li et al. [28] investigated the microstructure for MAO coating on the 6061 aluminum alloy in the $\text{Na}_2\text{SiO}_3\text{-CH}_3\text{COONa-Na}_5\text{P}_3\text{O}_{10}$ electrolyte system. The results showed that the size of spark was exponentially related to thickness of coating, and the structure of the coating was in a three-dimensional network. Du et al. [29] developed a black MAO coating on 2A12 aluminum alloy and found that the coating has superior adhesion and corrosion resistance. This will provide further research direction for developing MAO black coating on aluminum and aluminum alloy. Nalivaiko et al. [30] investigated the preparation of aluminum hydroxide obtained by aluminum anodic oxidation. The coating formed on high purity alumina consists of 4 stages from $\text{Al(OH)}_3\text{-NH}_4\text{Cl-H}_2\text{O}$ to $\alpha\text{-Al}_2\text{O}_3$.

In this paper, alumina coatings on 5083 aluminum alloy were prepared by MAO and anodic oxidation, respectively. The microstructure, elemental composition, and the corrosion behaviors of the two coatings were investigated. At the end, the corrosion mechanism of the two coatings was discussed in brief.

2. Experimental

The cyclone filter used in this work is made of commercial 5083 aluminum alloy. The chemical compositions of the commercial 5083 aluminum alloy are shown in Table 1. Prior to the experiments, the specimen was cut in pieces with dimensions of $60 \times 55 \times 3$ mm. The geometrical schematic diagram of the cyclone filter is shown in Figure 1.

Microarc oxidation and anodic oxidation techniques were used to prepare the coatings surface on the experimental samples of the cyclone filter, and the surface sealing treatment of the microarc oxidation coating was performed with 5% saline solution. Samples of the cyclone filter with the microarc oxidation treatment and the anodic oxidation treatment are shown in Figure 2.

The electrochemical response of MAO coating, anodic oxidation coating, and 5083 aluminum alloy was obtained using IM6/IM6e electrochemical workstation (ZAHNER, Germany) in 3.5 wt.% NaCl solution. A classic three-electrode system is used, which composed of a saturated Ag/AgCl reference electrode, a platinum sheet with dimensions of $20 \times 20 \times 0.1$ mm, and 5083 aluminum alloy and coatings as a working electrode [31]. The potentiodynamic polarization curves were conducted by sweeping the potential from $-0.6 \text{ V}/_{\text{Ag/AgCl}}$ below open circuit potential (OCP) with a scanning rate of 0.333 mV/s . The electrochemical impedance spectroscopy (EIS) tests were

TABLE 1: Chemical compositions of the 5083 aluminum alloy (wt.%).

Cu	Si	Mg	Zn	Fe	Cr	Ti	Mn	Al
0.09	0.31	4.1	0.21	0.35	0.05	0.05	0.47	Bal.

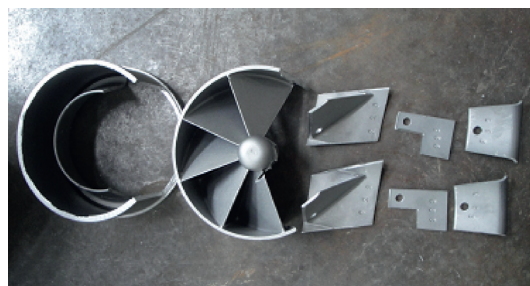


FIGURE 1: Test trial sample of cyclone separator.

performed at OCP with a sinusoidal potential perturbation of 10 mV in a frequency range from 10 kHz to 10 mHz. The tested solution was maintained at $25 \pm 1^\circ\text{C}$ in the air without stirring.

The salt spray test for MAO and anodic oxidation coating on 5083 aluminum alloy was conducted using machine DJS-EN61 according to the ISO 14993:2001 standard. The solution is 5 wt.% NaCl solution, pH of salt solution is 6.8, the temperature of the salt solution barrel is 35°C , and the sample place angle is 25° . The examination of the specimen was performed after 63 days of experiment. After the test, the samples were cleaned by flow water of temperature not higher than 35°C to remove the sample surface residual salt spray solution and then dried using hot air.

3. Result and Discussion

3.1. Surface Characterization of the Two Different Coatings. Figure 3 shows the surface morphologies of the MAO coating on 5083 aluminum alloy samples, revealing volcano-like morphologies with micropores of various sizes that can be observed on the surface. As is seen from Figure 3, the micropores are smaller in size with diameters of $2 \mu\text{m}$ and distributed uniformly. This is the characteristic of MAO coatings obtained by microsparks on the sample surface of alloys [25, 32]. Still some of the pores in the MAO are blocked. In Figure 3, the number of small white particles identified by EDS is Fe-rich particles. This is consistent with the finding of Chen [25]. In addition, no crack exists in Figure 3, which indicates that the MAO coating is very adhesive to 5083 aluminum alloy substrate [33].

The surface morphologies of anodic oxidation coating formed on 5083 aluminum alloy are shown in Figure 4. The anodic oxidation coating surface looks very dense, but there are a lot of cracks staggered on the surface. It could be seen that numerous wrinkles and cracks staggered on the surface. So, the corrosion properties would deteriorate due to these cracks.

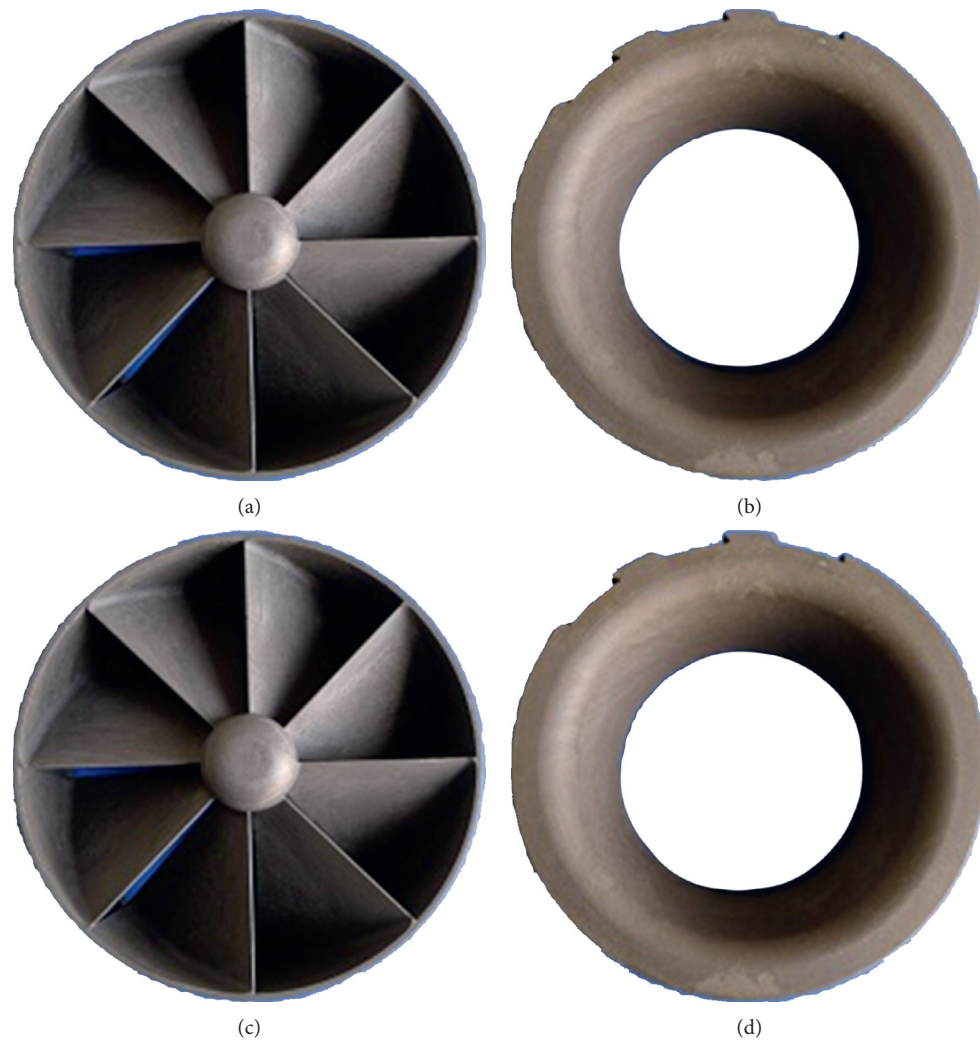


FIGURE 2: Marine cyclone separator structure sample by MAO and anodic oxidation: (a) MAO forward view; (b) MAO backward view; (c) anodic oxidation forward view; (d) anodic oxidation backward view.

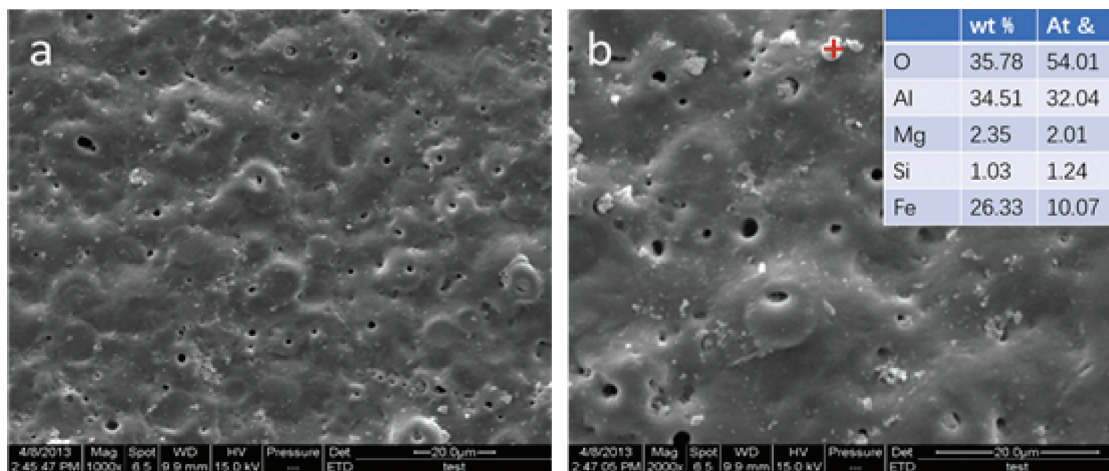


FIGURE 3: Surface morphologies of the MAO coatings.

3.2. *Potentiodynamic Polarization Curves.* The potentiodynamic polarization curves for MAO coating, anodic oxidation coating, and 5083 aluminum alloy in 3.5 wt.% NaCl

solution are shown in Figure 5. The curves indicated that the MAO coating and anodic oxidation coatings lead to the changes in the anodic current, pitting potential (E_{pit}), and

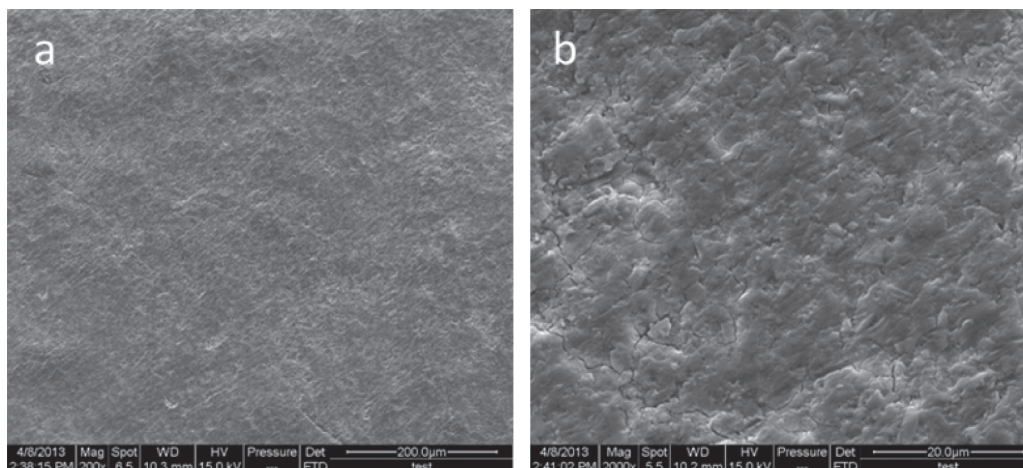


FIGURE 4: Surface morphologies of anodic oxidation coating.

corrosion rate. The potentiodynamic polarization curves indicated that the corrosion resistance of the MAO and anodic oxidation coatings can be significantly improved compared to the 5083 aluminum alloy matrix. It was obvious that MAO coating and anodic oxidation coating led to the positive shift in corrosion potential.

The corrosion potential (E_{corr}) of the 5083 aluminum alloy, anodic coating, and MAO coating is -694 ± 8 , -636 ± 12 , and -385 ± 11 mV/Ag/AgCl. Compared with the 5083 aluminum alloy, the corrosion potentials shifted nobly for the MAO and anodic oxidation coatings. The corrosion current density (i_{corr}) value of the 5083 aluminum alloy, anodic coating, and MAO coating is $3.33 \pm 0.11 \times 10^{-6}$, $7.33 \pm 0.24 \times 10^{-7}$, and $1.07 \pm 0.18 \times 10^{-9}$ A/cm², respectively. This suggests that the corrosion resistance for MAO coating is two orders higher than that for 5083 aluminum alloy. This indicates that both of the MAO and anodic oxidation coatings can reduce the corrosion rate of the 5083 aluminum alloy specimens in 3.5 wt.% NaCl solution [34–36].

3.3. Electrochemical Impedance Spectroscopy

3.3.1. MAO Coating. The Bode (Figure 6(a)) and Nyquist (Figure 6(b)) plots for MAO coating on 5083 aluminum alloy after immersion in 3.5 wt.% NaCl solution for 1 day are presented in Figure 6. The Nyquist plots exhibit two capacitive semicircles, suggesting the inductive behavior [34, 37]. Figure 7 presents the equivalent circuit used to simulate the EIS data, in which R_s is the resistance of the 3.5 wt.% NaCl solution and C_{dl} and R_{dl} are the capacitance and resistance of the adsorption layer, respectively. CPE and R_p are the capacitance and polarization resistance of the MAO coating, respectively. The use of a constant phase element (CPE) was used in place of capacitance because of the distribution of relaxation times resulting from heterogeneities at the electrode surface [31, 33, 38, 39]. The fitted parameters in the equivalent circuit in Figure 7 are given in Table 2.

The Bode (Figure 8(a)) and Nyquist (Figure 8(b)) plots for MAO coating on 5083 aluminum alloy after immersion

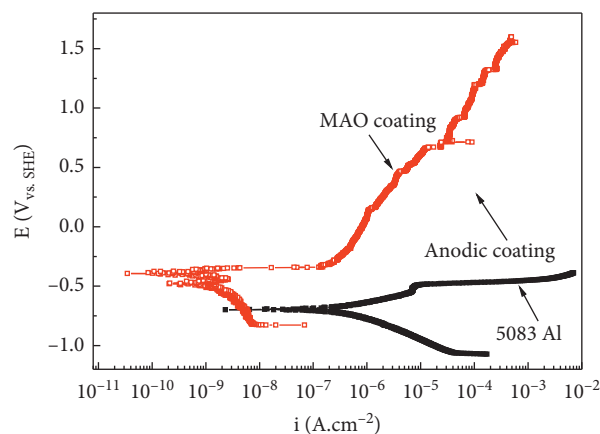


FIGURE 5: Potentiodynamic polarization curves for MAO coating, anodic oxidation coating, and 5083 aluminum alloy in 3.5 wt.% NaCl solution.

in 3.5 wt.% NaCl solution for 12 days are presented in Figure 8. The Nyquist plots exhibit a capacitive semicircle in high-frequency region and an inductive loop in low-frequency region [19]. The capacitive reactance arc corresponds to the process of ions passing through the MAO coating, and the inductive arc corresponds to the desorption process of the adsorbed intermediate products [40–42]. Figure 9 presents the equivalent circuit used to simulate the EIS data, in which CPE_f is the capacitance of the MAO coating, R_{pore} is the resistance of defects, C_{dl} is the double layer capacitance, R_p is the polarization resistance, L is the inductive resistance, and R_L is the inductive resistance, which is related to the active dissolution of MAO coating [43]. The fitted parameters in the equivalent circuit in Figure 9 are given in Table 3.

The Bode (a) and Nyquist (b) plots for MAO or 32 and 63 days are presented in Figure 10. The Nyquist plots exhibit a capacitive semicircle and a bias line at low-frequency region. The capacitive reactance arc corresponds to the process of ions passing through the MAO coating [43]. The bias line at low frequency corresponds to the diffusion process of Cl^-

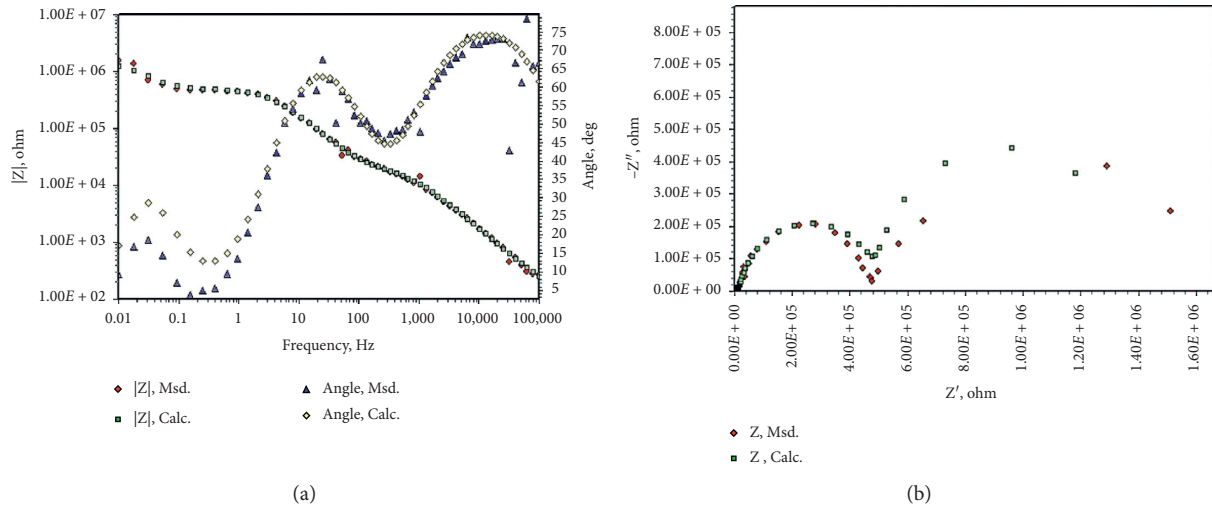


FIGURE 6: (a) Bode and (b) Nyquist curves of MAO coating after being immersed in 3.5 wt.% NaCl solution for 1 day.

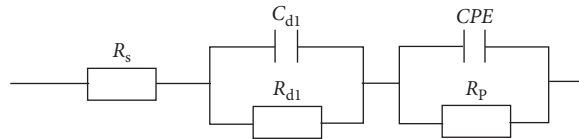


FIGURE 7: The equivalent circuit used to evaluate the EIS data presented in Figure 8.

TABLE 2: Fitting results of the equivalent circuit obtained by fitting the EIS data.

R_s ($\Omega \cdot \text{cm}^{-2}$)	R_{d1} ($\Omega \cdot \text{cm}^{-2}$)	C_{d1} ($\text{F} \cdot \text{cm}^{-2}$)	Y_0 ($\Omega^{-1} \text{s}^n \text{cm}^{-2}$)	n	R_p ($\Omega \cdot \text{cm}^{-2}$)
3.14	4.28×10^4	1.37×10^{-5}	2.91×10^{-5}	0.85	7.16×10^5

Note: Y_0 : CPE constant; n : CPE exponent.

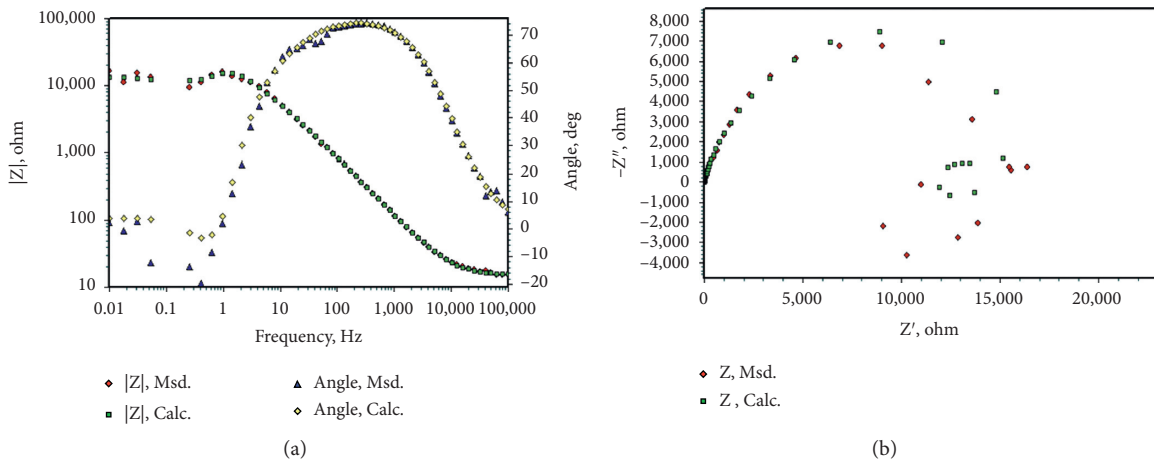


FIGURE 8: (a) Bode and (b) Nyquist curves of MAO coating after being immersed in 3.5 wt.% NaCl solution for 12 days.

through the MAO coating [44]. Figure 11 presents the equivalent circuit used to simulate the EIS data, in which W is the Warburg impedance. W was used to fit the data of MAO coating suggesting the responses induced by diffusion in paths of semi-infinite length [43, 44]. The fitted

parameters in the equivalent circuit in Figure 11 are given in Table 4.

From the EIS response, it can be inferred that three stages for MAO coating during the immersion time can be identified. In the first stage, the equivalent circuit in Figure 7

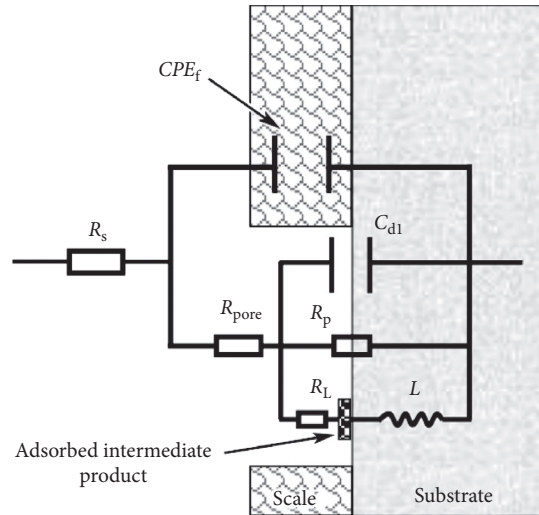


FIGURE 9: Equivalent circuit used to evaluate the EIS data presented in Figure 10 (Figure 9 is reproduced from [42] under the Creative Commons Attribution License/public domain).

TABLE 3: Fitting results of the equivalent circuit obtained by fitting the EIS data.

R_s ($\Omega \cdot \text{cm}^{-2}$)	Y_0 ($\Omega^{-1} \cdot \text{s}^n \cdot \text{cm}^{-2}$)	n	R_{pore} ($\Omega \cdot \text{cm}^{-2}$)	C_{dl} ($\text{F} \cdot \text{cm}^{-2}$)	R_p ($\Omega \cdot \text{cm}^{-2}$)	L ($\text{H} \cdot \text{cm}^{-2}$)	R_L ($\Omega \cdot \text{cm}^{-2}$)
7.42	5.19×10^{-4}	0.89	5.18×10^2	4.57×10^{-5}	7.21×10^5	3.21×10^2	4.50×10^4

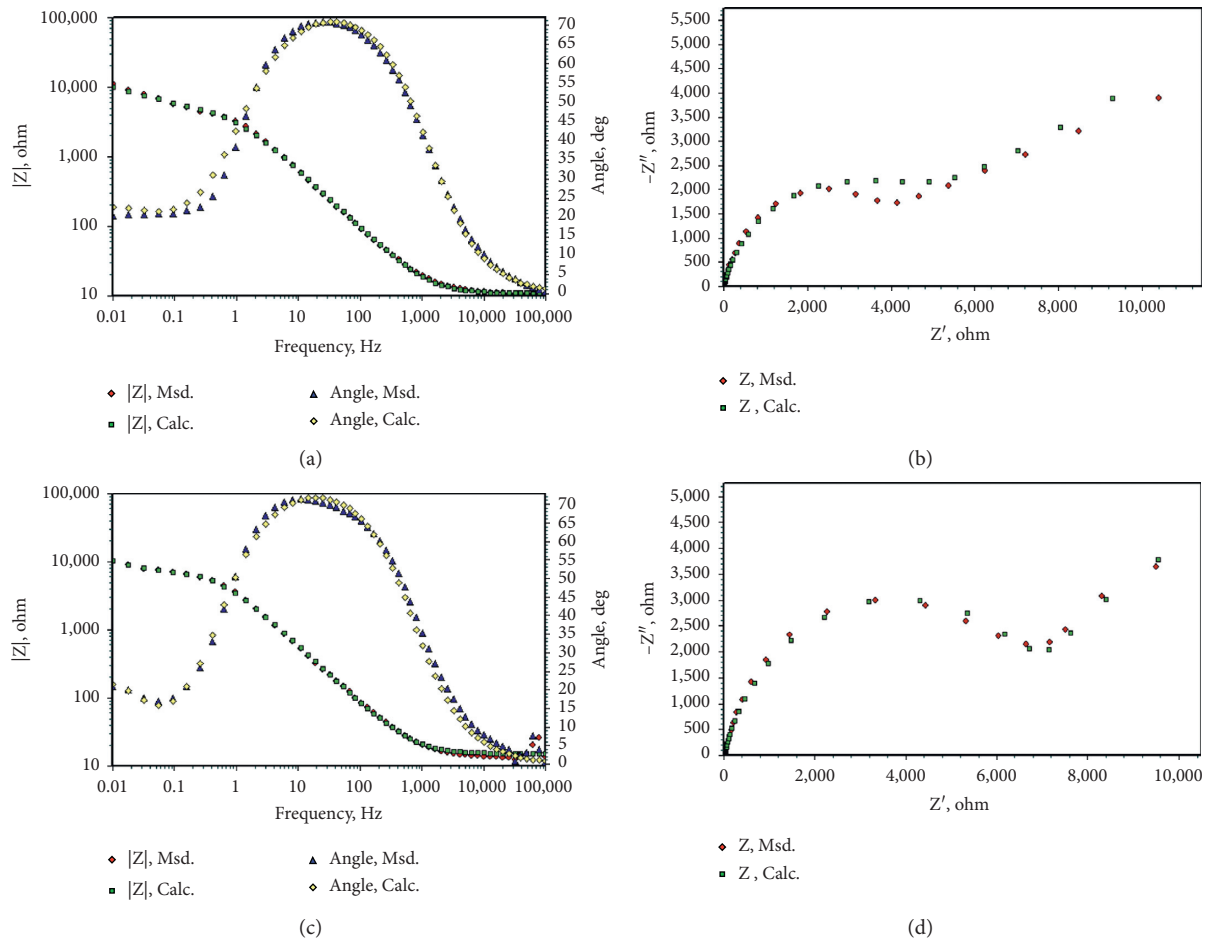


FIGURE 10: (a) Bode and (b) Nyquist curves of MAO coating after being immersed in 3.5 wt.% NaCl solution for 32 and 63 days.

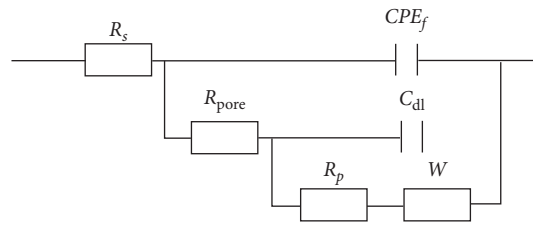
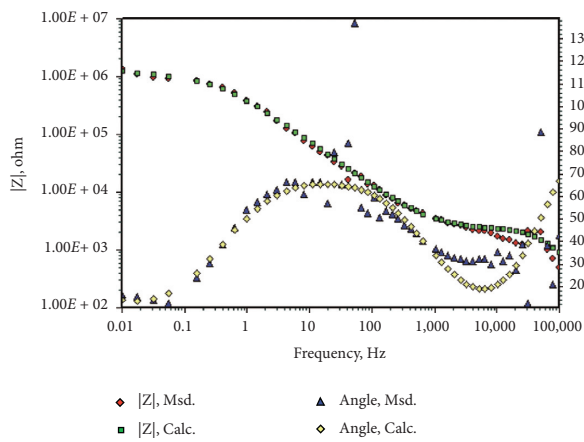


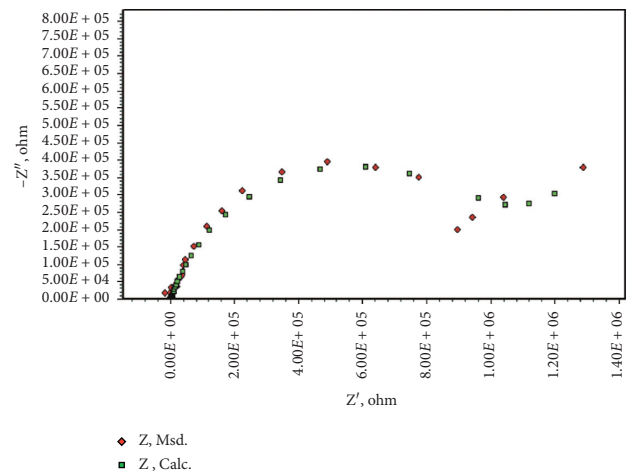
FIGURE 11: Equivalent circuit used to evaluate the EIS data presented in Figure 10.

TABLE 4: Fitting results of the equivalent circuit obtained by fitting the EIS data.

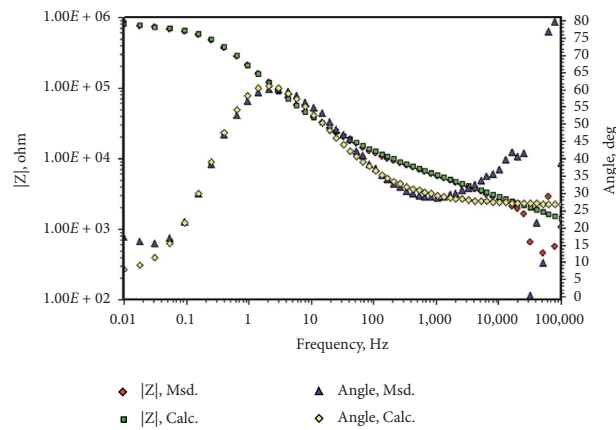
R_s ($\Omega \cdot \text{cm}^{-2}$)	Y_0 ($\Omega^{-1} \cdot \text{s}^n \cdot \text{cm}^{-2}$)	N	R_{pore} ($\Omega \cdot \text{cm}^{-2}$)	C_{dl} ($\text{F} \cdot \text{cm}^{-2}$)	R_p ($\Omega \cdot \text{cm}^{-2}$)	W ($\text{s}^{-0.5} \Omega \cdot \text{cm}^{-2}$)
6.13	2.16×10^{-5}	0.85	1.78×10^3	1.57×10^{-5}	7.16×10^5	3.21×10^{-2}



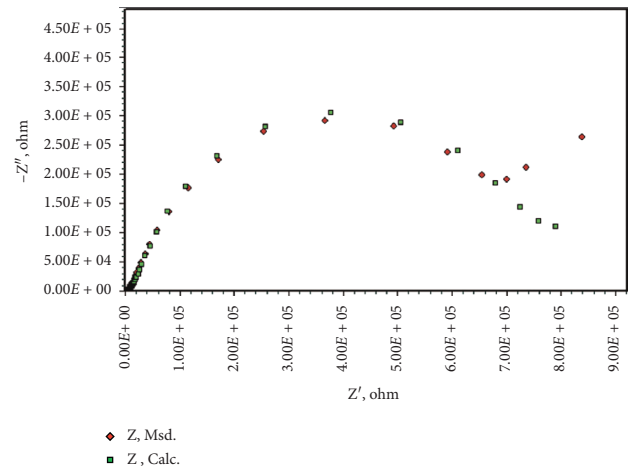
(a)



(b)



(c)



(d)

FIGURE 12: Continued.

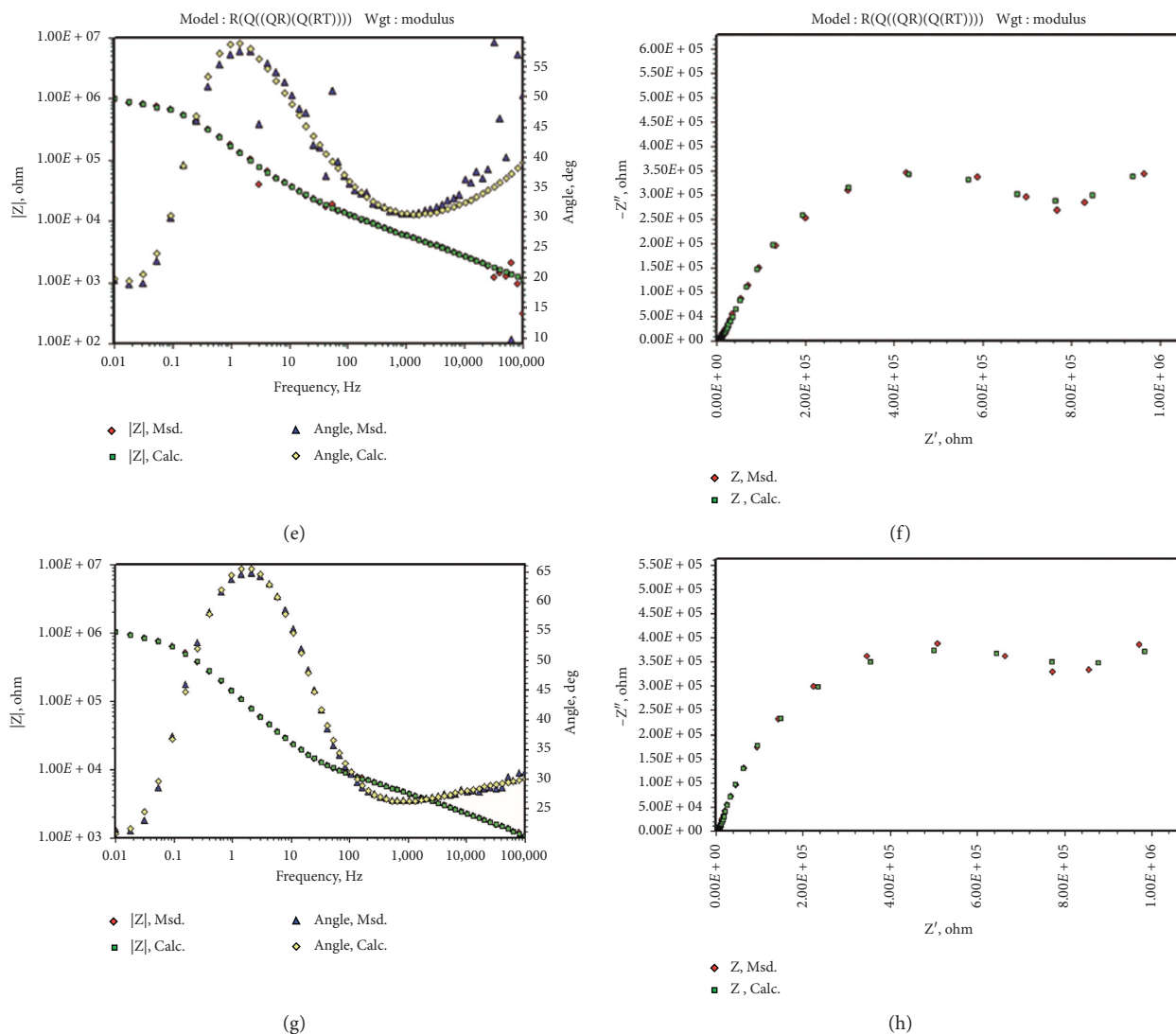


FIGURE 12: Bode and Nyquist curves of anodic oxidation coating after being immersed in 3.5 wt.% NaCl solution for (a, b) 1 day, (c, d) 12 days, (e, f) 32 days, and (g, h) 63 days.

indicates that the MAO has superior corrosion protection ability. In the second stage, identifying at increasing immersion time, the EIS presents desorption characteristics at low frequencies connecting to a capacitive semicircle at high frequencies (Figure 9). In this stage, local pitting corrosion in the MAO coating takes place stimulating Al matrix dissolution through corrosion pits [45]. After long immersion time, the chloride effectively induces local breakdown of the MAO coating, which is in agreement with the reported findings in the literature. The chloride ion may penetrate through the MAO coating and reach matrix/coating interface. As a result, an additional Warburg impedance at low frequency is employed.

3.3.2. Anodic Oxidation Coating. The EIS plots for anodic oxidation coating on 5083 aluminum alloy after immersion in 3.5 wt.% NaCl solution for 1, 12, 32, and 63 days are

presented in Figure 12. The Warburg impedance in Figure 11 is due to the existence of cracks (Figure 3(b)), which can act as the diffusion path for the corrosive ions. The equivalent circuit used to interpret the EIS data is shown in Figure 12. The fitted parameters obtained are given in Table 5. As is seen from Table 5, the value of R_p decreased with the increase in immersion time. It indicated that the protective performance of the anodic oxidation coating on 5083 aluminum alloy surface deteriorated and the risk of corrosion increased [45, 46].

3.4. Salt Spray Test. Figure 13 shows the surface morphologies of the two different coatings on 5083 aluminum alloy after the salt spray test for 63 days. The breakdown of the both coatings is not visible observed. As is seen from Figure 13, there are almost no signs of corrosion on the surface of MAO coating. However, there was slight corrosion on

TABLE 5: Fitting results of the equivalent circuit obtained by fitting the EIS data.

Time (days)	R_s ($\Omega\cdot\text{cm}^{-2}$)	Y_0 ($\Omega^{-1}\cdot\text{s}^n\cdot\text{cm}^{-2}$)	n	R_{pore} ($\Omega\cdot\text{cm}^{-2}$)	C_{dl} ($\text{F}\cdot\text{cm}^{-2}$)	R_p ($\Omega\cdot\text{cm}^{-2}$)	W ($\text{s}^{-0.5}\Omega\cdot\text{cm}^{-2}$)
1	4.32	7.57×10^{-5}	0.94	4.38×10^2	1.57×10^{-5}	9.81×10^5	3.89×10^{-2}
12	5.61	6.42×10^{-5}	0.92	4.05×10^2	2.44×10^{-5}	7.65×10^5	4.77×10^{-2}
32	6.35	7.70×10^{-5}	0.91	3.89×10^2	1.84×10^{-5}	7.03×10^5	6.25×10^{-2}
63	4.28	6.82×10^{-5}	0.89	3.45×10^2	2.06×10^{-5}	6.41×10^5	7.03×10^{-2}

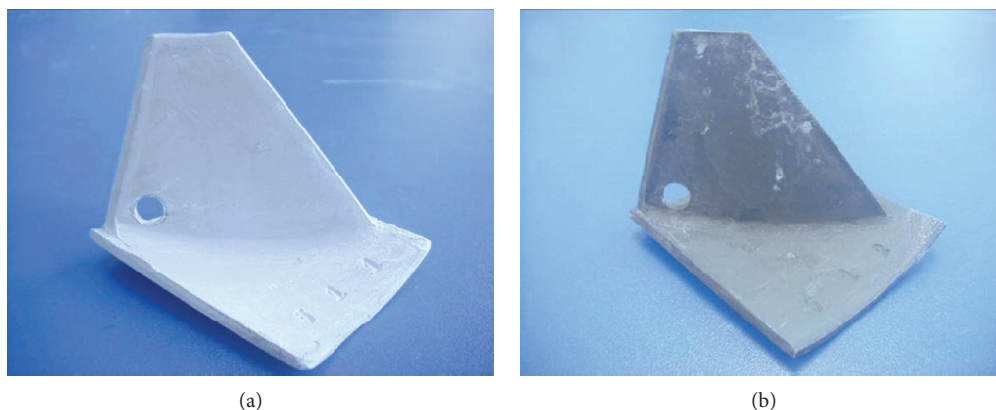


FIGURE 13: Surface morphology of the (a) MAO coating and (b) anodic oxidation coating after the salt spray test.

anodic oxidation coating. This is in good agreement with the electrochemical measurement.

4. Conclusions

The protective performance of the MAO is superior than that of the anodic oxidation coating. The 5083 aluminum alloy with MAO coating showed a good corrosion resistance at the initial stage. With the increase in immersion time, the pitting corrosion occurs in the MAO coating, and the protective ability of the coating deteriorated gradually. In contrast, the existence of the cracks in anodic oxidation coating can act as the diffusion path for the corrosive ions. The corrosion process is controlled by ion diffusion throughout the coatings.

Data Availability

The data used to support the findings of this study are available from the corresponding author upon request.

Conflicts of Interest

The authors declare that they have no conflicts of interest.

Acknowledgments

This research was funded by the National Natural Science Foundation of China (nos. 51679051 and 51701050), the Outstanding Youth Foundation of Heilongjiang Province

(YQ2019E015), and the National Science and Technology Major Project (2017-V-0002-0051).

References

- [1] X. Z. Xie, "Air inlet treatment quality to influencing on the gas turbine," *Turbine Technology*, vol. 3, pp. 226–229, 2007.
- [2] R. Kurz and K. Brun, "Degradation in gas turbine systems," in *Proceedings of the ASME Turbo Expo 2000: Power for Land, Sea, and Air*, Munich, Germany, May 2000.
- [3] S. C. Fu, G. G. Sun, and C. Z. Gao, "Research and application status of guide vanes uniflow cyclone," *Journal of Filtration & Separation*, vol. 18, no. 2, pp. 11–14, 2008.
- [4] L. Shuyan, L. Ying, L. Fuqing, H. Hongbin, and Y. Weige, "Experimental research on the filtering efficiency for a new style of air filter," *Journal of Beijing Institute of Technology*, vol. 19, no. 2, pp. 171–175, 2000.
- [5] J. P. Vander Walt and A. Nurick, "Erosion of dust-filtered helicopter turbine engine Part I: basic theoretical consideration," *Journal of Aircraft*, vol. 32, no. 1, pp. 105–111, 1995.
- [6] Z. Liu, Z. Xu, and C. Zhang, "A study of the corrosion-resistant characteristics of the blades of a compressor and their protective coatings," *Journal Of Engineering for Thermal Energy and Power*, vol. 22, no. 5, pp. 490–494, 2007.
- [7] W. J. Huo and H. G. Sun, "Corrosion and precaution for blades of aero-engine compressor in the navy air arm," *Aviation Engineering & Maintenance*, vol. 6, pp. 39–41, 2002.
- [8] H. O. Sun, H. T. Zheng, and S. L. Liu, "Numerical simulation of resistance characteristics of multilayer gauze stage in moisture separator," *Journal of Harbin Engineering University*, vol. 21, no. 8, pp. 10–12, 2000.

- [9] T. Zong, D. M. Hu, and J. Li, "Numerical simulation of cyclonic separator in circulating fluidized bed boiler with CFD," *Journal of Shanghai University of Electric Power*, vol. 3, 2011.
- [10] A. P. Tarabine, V. A. Schurovasky, A. I. Bodrov, and J.-P. Stalder, "An analysis of axial compressor fouling and a cleaning method of their blading," in *Proceedings of the ASME 1996 International Gas Turbine and Aeroengine Congress and Exhibition*, Birmingham, UK, June 1996.
- [11] W. D. Griffiths and F. Boysan, "Computational fluid dynamics (CFD) and empirical modelling of the performance of a number of cyclone samplers," *Journal of Aerosol Science*, vol. 27, no. 2, pp. 281–304, 1996.
- [12] Z. Xu, "The coating preparation of turbine compressor vane in the ship and the research of anti-corrosion and wear-resistant properties," Master's thesis, Harbin Engineering University, Harbin, China, 2006.
- [13] Z.-P. Shi, Z.-B. Wang, J.-Q. Wang et al., "Effect of Ni interlayer on cavitation erosion resistance of NiTi cladding by tungsten inert gas (TIG) surfacing process," *Acta Metallurgica Sinica (English Letters)*, vol. 33, no. 3, pp. 415–424, 2020.
- [14] G. Grant and W. Tabakoff, "Erosion prediction in turbo machinery from environmental solid articles," *Journal of Aircraft*, vol. 12, pp. 471–478, 1975.
- [15] W. S. Kim and J. W. Lee, "Collection efficiency model based on boundary-layer characteristics for cyclones," *AIChE Journal*, vol. 43, no. 10, pp. 2446–2455, 1997.
- [16] J. J. H. Brouwers, "Particle collection efficiency of the rotational particle separator," *Powder Technology*, vol. 92, no. 2, pp. 89–99, 1997.
- [17] Y. Z. Zhang, H. G. Hu, and Z. Y. Liu, "Experimental research on the axial multi-stage cyclone separator," *Industrial Boiler*, vol. 4, 1997.
- [18] M. Esmaily, N. Mortazavi, W. Osikowicz et al., "Corrosion behaviour of friction stir-welded AA6005-T6 using a bobbin tool," *Corrosion Science*, vol. 111, pp. 98–109, 2016.
- [19] Y. X. Qiao, Y. Zhou, S. J. Chen, and Q. N. Song, "Effect of bobbin tool friction stir welding on microstructure and corrosion behavior of 6061-T6 aluminum alloy joint in 3.5% NaCl solution," *Acta Metallurgica Sinica*, vol. 52, no. 11, pp. 1395–1402, 2016.
- [20] L. Lokas and V. Alar, "The effect of temperature on corrosion behavior of AA5083 in brackish water and seawater," *Materials and Corrosion*, vol. 70, no. 10, pp. 1817–1825, 2019.
- [21] K. A. Yasakau, M. L. Zheludkevich, S. V. Lamaka, and M. G. S. Ferreira, "Role of intermetallic phases in localized corrosion of AA5083," *Electrochimica Acta*, vol. 52, no. 27, pp. 7651–7659, 2007.
- [22] Z. Peng, Q. Pan, S. Cai, J. Li, and W. Liang, "Effect of different aging processes on the corrosion behavior of new Al-Cu-Li-Zr-Sc alloys," *Materials and Corrosion*, vol. 70, no. 12, pp. 2266–2277, 2019.
- [23] F. Sun, X. Li, L. Lu, X. Cheng, C. Dong, and J. Gao, "Corrosion behavior of 5052 and 6061 aluminum alloys in deep ocean environment of south China sea," *Acta Metallurgica Sinica*, vol. 49, no. 10, pp. 1219–1226, 2013.
- [24] Y. K. Wang, L. Sheng, R. Z. Xiong, and B. S. Li, "Study of ceramic coatings formed by microarc oxidation on Al matrix composite surface," *Surface Engineering*, vol. 15, no. 2, pp. 112–114, 1999.
- [25] M.-A. Chen, Y.-C. Ou, Y.-H. Fu, Z.-H. Li, J.-M. Li, and S.-D. Liu, "Effect of friction stirred Al-Fe-Si particles in 6061 aluminum alloy on structure and corrosion performance of MAO coating," *Surface and Coatings Technology*, vol. 304, pp. 85–97, 2016.
- [26] M. M. Krishtal, "Effect of structure of Aluminum-Silicon alloys on the process of formation and characteristics of oxide layer in microarc oxidizing," *Metal Science and Heat Treatment*, vol. 46, no. 9, pp. 378–384, 2004.
- [27] S. Xin, L. Song, R. Zhao, and X. Hu, "Influence of cathodic current on composition, structure and properties of Al₂O₃ coatings on aluminum alloy prepared by micro-arc oxidation process," *Thin Solid Films*, vol. 515, no. 1, pp. 326–332, 2006.
- [28] X. Y. Li, X. G. Li, Y. Li et al., "Growth mechanism of micro-arc oxidation film on 6061 aluminum alloy," *Materials Research Express*, vol. 6, no. 6, Article ID 066404, 2019.
- [29] C. Du, H. Zhao, Z. Dai, Z. Tian, J. Wang, and Z. Wang, "The preparation and properties of black coating by micro arc oxidation on 2A12 aluminum alloy," *Materials Letters*, vol. 236, pp. 723–726, 2019.
- [30] A. Y. Nalivaiko, D. Y. Ozherelkov, V. I. Pak, S. S. Kirov, A. N. Arnautov, and A. A. Gromov, "Preparation of aluminum hydroxide during the synthesis of high purity alumina via aluminum anodic oxidation," *Metallurgical and Materials Transactions B*, vol. 51, no. 3, pp. 1154–1161, 2020.
- [31] Z. B. Wang, H. X. Hu, Y. G. Zheng, W. Ke, and Y. X. Qiao, "Comparison of the corrosion behavior of pure titanium and its alloys in fluoride-containing sulfuric acid," *Corrosion Science*, vol. 103, pp. 50–65, 2016.
- [32] R. F. Zhang, W. H. Chang, L. F. Jiang et al., "Formation of microcracks during micro-arc oxidation in a phytic acid-containing solution on two-phase AZ91HP," *Journal of Materials Engineering and Performance*, vol. 25, no. 4, pp. 1304–1316, 2016.
- [33] Y. X. Qiao, J. Huang, D. Huang et al., "Effects of laser scanning speed on microstructure, microhardness and corrosion behavior of laser cladding Ni45 coatings," *Journal of Chemistry*, vol. 2020, p. 11, Article ID 1438473, 2020.
- [34] L. M. Zhang, M. C. Yan, S. D. Zhang et al., "Significantly enhanced resistance to SRB corrosion via Fe-based amorphous coating designed with high dose corrosion-resistant and antibacterial elements," *Corrosion Science*, vol. 164, p. 9, Article ID 108305, 2020.
- [35] S. Hong, Y. Wu, J. Wu et al., "Microstructure and cavitation erosion behavior of HVOF sprayed ceramic-metal composite coatings for application in hydro-turbines," *Renewable Energy*, vol. 164, pp. 1089–1099, 2021.
- [36] Y. X. Qiao, Z. H. Tian, X. Cai et al., "Cavitation erosion behaviors of a nickel-free high-nitrogen stainless steel," *Tribology Letters*, vol. 67, no. 1, pp. 1–9, 2019.
- [37] A. Carnot, I. Frateur, S. Zanna, B. Tribollet, I. Dubois-Brugger, and P. Marcus, "Corrosion mechanisms of steel concrete moulds in contact with a demoulding agent studied by EIS and XPS," *Corrosion Science*, vol. 45, no. 11, pp. 2513–2524, 2003.
- [38] C. Jeyaprabha, S. Sathiyarayanan, and G. Venkatachari, "Influence of halide ions on the adsorption of diphenylamine on iron in 0.5M H₂SO₄ solutions," *Electrochimica Acta*, vol. 51, no. 19, pp. 4080–4088, 2006.
- [39] Y. Qiao, D. Xu, S. Wang et al., "Effect of hydrogen charging on microstructural evolution and corrosion behavior of Ti-4Al-2V-1Mo-1Fe alloy," *Journal of Materials Science & Technology*, vol. 60, pp. 168–176, 2021.
- [40] C. F. Chen, M. X. Lu, G. X. Zhao, Z. Q. Bai, M. L. Yan, and Y. Q. Yang, "Effects of temperature, Cl concentration and Cr on electrode reactions of CO₂ N80 steel," *Acta Metallurgica Sinica*, vol. 39, no. 8, pp. 848–854, 2003.
- [41] M. Keddam, O. R. Mottos, and H. Takenouti, "Reaction model for iron dissolution studied by electrode impedance: I .

- experimental results and reaction model,” *Journal of The Electrochemical Society*, vol. 128, no. 2, pp. 257–266, 1981.
- [42] Y. D. Li, Q. Li, X. Tang, and Y. Li, “Reconstruction and characterization of galvanic corrosion behavior of X80 pipeline steel welded joints,” *Acta Metallurgica Sinica*, vol. 55, no. 6, pp. 801–810, 2019.
- [43] L. Calabrese, A. Capri, F. Fabiano, L. Bonaccorsi, C. Borsellino, and E. Proverbio, “Electrochemical behaviour in synthetic saliva of silane coated Ni/Cu/Ni Nd-Fe-B magnet for dentistry applications,” *Materials and Corrosion*, vol. 67, no. 5, pp. 484–494, 2016.
- [44] P. Salehikahrizangi, K. Raeissi, F. Karimzadeh, L. Calabrese, S. Patane, and E. Proverbio, “Erosion-corrosion behavior of highly hydrophobic hierarchical nickel coatings,” *Colloids and Surfaces A: Physicochemical and Engineering Aspects*, vol. 558, pp. 446–454, 2018.
- [45] S. Mao, H. Yang, Z. Song, J. Li, H. Ying, and K. Sun, “Corrosion behaviour of sintered NdFeB deposited with an aluminium coating,” *Corrosion Science*, vol. 53, no. 5, pp. 1887–1894, 2011.
- [46] S. Cui, J. Han, Y. Du, and W. Li, “Corrosion resistance and wear resistance of plasma electrolytic oxidation coatings on metal matrix composites,” *Surface and Coatings Technology*, vol. 201, no. 9-11, pp. 5306–5309, 2007.